

# Local Symmetry Breaking Induced Superionic Conductivity in Argyrodites

Te Kang,<sup>II</sup> Changyuan Li,<sup>II</sup> Xinjue Zhang, Yuiga Nakamura, Jo-chi Tseng, Taishun Manjo, Chaofeng Liu, and Long Yang<sup>\*</sup>



Cite This: <https://doi.org/10.1021/jacs.5c17193>



Read Online

ACCESS |

Metrics & More

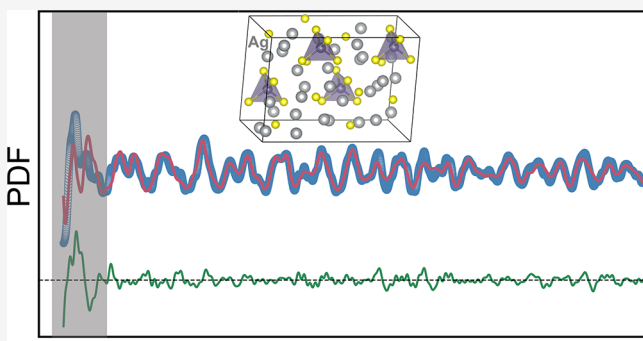


Article Recommendations



Supporting Information

**ABSTRACT:** Argyrodites have complex crystal structures that give rise to extraordinary physical properties, including ultralow thermal conductivity and superior ionic conductivity, which have received wide interest in thermoelectric materials and rechargeable batteries. While the long-range crystallographic structures of argyrodites have been well characterized, the local atomic-scale structural features remain poorly understood. In this work, synchrotron X-ray atomic pair distribution function (PDF) analysis has been carried out to investigate the short-range structural correlations in  $\text{Ag}_8\text{GeS}_6$  argyrodites and their structure evolution with temperature. Strikingly, the local atomic arrangement shares similarity across the superionic phase transition, and the phenomenon is further validated in other Ag-based argyrodites. Our analysis reveals that the local structural distortion, weak bonding environment, and strong lattice anharmonicity could be the key to understanding the exotic thermal and ion transport behavior. This work explores the critical connection between local structural motifs and macroscopic functionalities in Ag-based argyrodites, proposing a new local-structure-oriented strategy for designing next-generation functional materials.



Interatomic distance

## 1. INTRODUCTION

Superionic materials have received significant attention in the field of all-solid-state batteries due to their exceptional ionic mobility.<sup>1,2</sup> Among them, one material family called argyrodites has been known for its high ionic conductivity at the high-temperature superionic phase, which can be classified by the general formula:  $A_{(12-n)/m} M^{n+} X_6^{2-}$  or  $A_{(12-n-x)/m} M^{n+} X_{6-x}^{2-} Y_x^-$  ( $0 \leq x \leq 1$ ) ( $A^{m+} = \text{Li}^+, \text{Cu}^+, \text{Ag}^+, M^{n+} = \text{Al}^{3+}, \text{Ga}^{3+}, \text{Si}^{4+}, \text{Ge}^{4+}, \text{Sn}^{4+}, \text{P}^{5+}$ ,  $X^{2-} = \text{S}^{2-}, \text{Se}^{2-}, \text{Te}^{2-}$  and  $Y^- = \text{Cl}^-, \text{Br}^-, \text{I}^-$ ).<sup>3,4</sup> Among these rich compounds, Li-based  $\text{Li}_6\text{PS}_5\text{X}$  ( $\text{X} = \text{Cl}, \text{Br}, \text{I}$ ) materials have been extensively studied as solid-state electrolytes.<sup>5-7</sup> Meanwhile, Ag/Cu-based argyrodites exhibit ultralow thermal conductivity, making them promising candidates for thermoelectric applications.<sup>8</sup> Notably, these Ag/Cu-based argyrodites have a temperature-independent and amorphous-like thermal conductivity both above and below the superionic phase transition, with an average lattice thermal conductivity of only 0.3 W/m·K at room temperature, as low as that of wood.<sup>9</sup>

Argyrodites exhibit complex crystal structures, and their low-temperature crystallographic structures vary significantly depending on their chemical compositions.<sup>10,11</sup> However, all the high-temperature phases retain the same cubic symmetry (space group  $F\bar{4}3m$ ), known as the superionic phase. Moreover, the phase transition varies significantly with the

stoichiometry, and some structure-related studies have shown that argyrodites undergo rich phase transitions.<sup>12-15</sup> Previous studies have tried to understand the thermal and electrical transport properties of these compounds, from the perspective of long-range crystalline structures,<sup>16,17</sup> such as weak cation bonding,<sup>18</sup> low phonon cutoff frequency,<sup>19</sup> and soft phonon behavior.<sup>12,13</sup> In addition, the crystal structure characteristics of the superionic phase could enable fast ion diffusion in the rigid framework, and high ionic conductivities have been reported in Ag/Cu-based argyrodites.<sup>14,20</sup> Though these Ag/Cu-based argyrodites exhibit certain degrees of ionic conductivity, the commonly high electronic conductivity hinders the application in solid electrolytes.

The thermal conductivity and ionic conductivity properties are highly related to atomic arrangements in crystal lattices. Correspondingly, phonon scattering and ion diffusion mechanisms are mainly determined by the local structural environment. Since phonons and ions move at adjacent sites, it

Received: September 30, 2025

Revised: January 1, 2026

Accepted: January 5, 2026

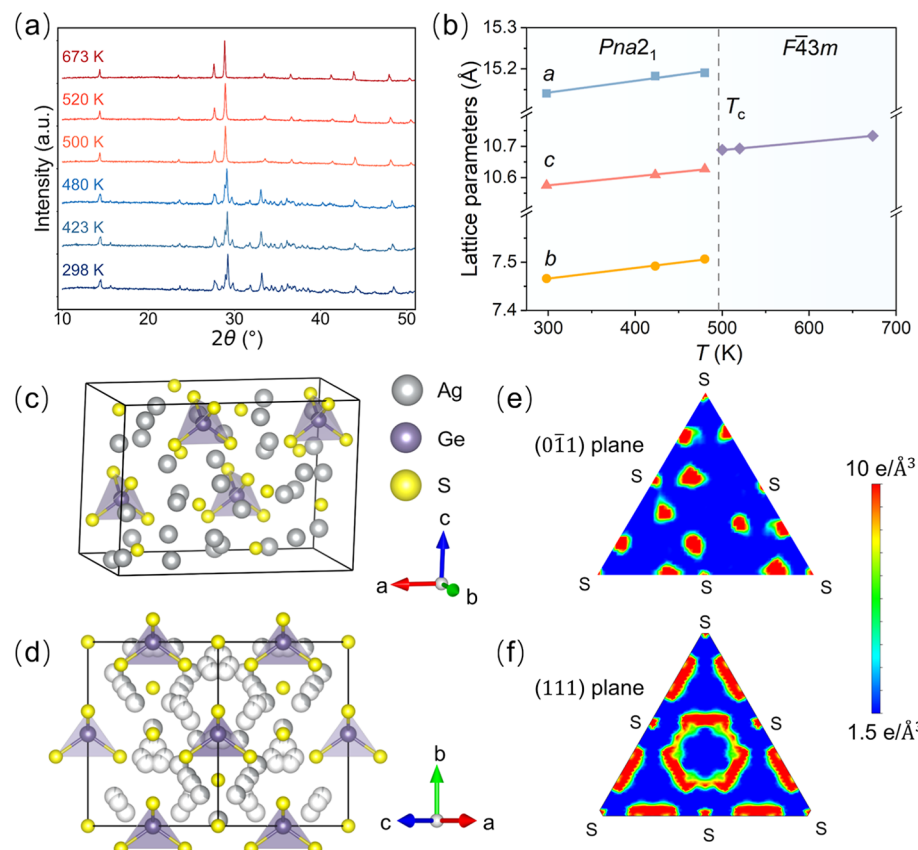


**Figure 1.** (a) Temperature-dependent XRD patterns of polycrystalline  $\text{Ag}_8\text{GeS}_6$  over 298–673 K. (b) Variation of the lattice parameters ( $a$ ,  $b$ ,  $c$ ) with increasing temperature as extracted from the powder XRD data. (c) Crystal structure of the low-temperature  $\text{Ag}_8\text{GeS}_6$  orthorhombic  $Pna2_1$  phase. Ag, Ge, and S atoms are represented by gray, purple, and yellow, respectively. (d) Crystal structure of the high-temperature  $\text{Ag}_8\text{GeS}_6$  cubic  $F\bar{4}3m$  phase. (e) The electron density distribution of low-temperature phase determined from MEM analysis at 298 K. (f) The electron density distribution of high-temperature phase determined from MEM analysis at 673 K. The (111) plane of high-temperature cubic  $F\bar{4}3m$  phase matches the (011) planes of low-temperature orthorhombic  $Pna2_1$  phase in (e).

is crucial to study the local structure beyond the well-known long-range crystallographic structure.

In this work, we used the total scattering based atomic pair distribution function (PDF) method to study the local structure of  $\text{Ag}_8\text{GeS}_6$ , which gives the interatomic distance distribution directly, i.e., the probability of finding atomic pairs of distance  $r$  apart.<sup>21,22</sup> The temperature-dependent synchrotron X-ray PDF data reveal local structure variations across the phase transition. Beyond the well-studied crystalline periodic structure, the three-dimensional diffuse scattering signals over the full reciprocal space were visualized directly by a newly developed three-dimensional X-ray total scattering characterization method.<sup>23,24</sup> This material exhibits electronic insulating properties along with moderate ionic conductivity, making it a promising candidate for solid-state electrolytes, which has been demonstrated in all solid-state batteries (ASSBs) successfully.

## 2. EXPERIMENTAL METHODS

### 2.1. X-ray Diffraction

The temperature-dependent laboratory X-ray diffraction (XRD) was measured by PANalytical Empyrean equipment ( $\text{Cu } K_{\alpha}$   $\lambda = 1.5406 \text{ \AA}$ ), and six temperature points were collected on heating in vacuum: 298, 423, 480, 500, 520, and 623 K, respectively. The GSAS-II software was used for XRD Rietveld refinements.<sup>25</sup>

### 2.2. Maximum Entropy Method Analysis

The electron density distributions were analyzed from the observed structure factor by the maximum entropy method (MEM), using the Dysnomia program.<sup>26,27</sup> The crystal structures and the electron density distribution iso-surfaces were visualized in VESTA.<sup>28</sup>

### 2.3. Atomic Pair Distribution Function

The experimental PDF, denoted  $G(r)$ , is the truncated Fourier transform of the total scattering structure function<sup>29,30</sup>

$$G(r) = \frac{2}{\pi} \int_{Q_{\min}}^{Q_{\max}} Q[S(Q) - 1] \sin(Qr) dQ$$

where  $Q$  is the magnitude of the scattering momentum transfer,  $S(Q)$  is the total scattering structure function extracted from the Bragg and diffuse components of X-ray powder diffraction intensity. The synchrotron X-ray total scattering measurements of  $\text{Ag}_8\text{GeS}_6$  were carried out at the BL02B1 and BL04B2 beamlines at Super Photon ring-8 GeV (SPring-8) in Japan. For other argyrodites, the X-ray PDF data were collected at the BL08W of SPring-8 and BL12SW of the Shanghai Synchrotron Radiation Facility (SSRF) in China. The PDF data processing and local structure analysis were performed by the pyFAI, PDFgetX3, and PDFgui programs.<sup>29–31</sup> Details of X-ray PDF experiments are introduced in the Supporting Information.<sup>32–34</sup>

### 2.4. Three-Dimensional Total Scattering

The three-dimensional synchrotron X-ray total scattering measurements were carried out at the BL02B1 beamline of SPring-8 with an incident beam energy of 50.0 keV, using a Pilatus 1 M detector. The data were collected with flowing  $\text{N}_2$  gas at 100, 200, and 300 K, respectively. The single crystal was rotated by  $180^\circ$  with  $0.1^\circ$  step.

The exposure time for each frame was 0.2 s. Three sets of rotation images were collected for the  $\text{Ag}_8\text{GeS}_6$  sample with the angle slightly changed at two distinct axes to fill in detector gaps. The resulting images were stacked into a three-dimensional array and transformed into reciprocal space coordinates using the software packages NXRefine and CCTW (Crystal Coordinate Transformation Workflow) within NeXpy.<sup>24,35</sup> The reciprocal space data covered a  $Q$  range of approximately  $\pm 15 \text{ \AA}^{-1}$  in all directions.

## 2.5. Inelastic X-ray Scattering

The inelastic X-ray scattering (IXS) experiments were performed at the BL35XU beamline of SPring-8.<sup>36</sup> A Si (11 11 11) backscattering setup with an energy resolution of 1.5 meV and an incident X-ray energy of 21.747 keV was chosen. The sample was mounted on the Cu holder. The IXS experiment was performed using the transmission geometry at room temperature. A 2D analyzer array was used in the experiments. The damped harmonic oscillator (DHO) model convoluted with the resolution function was applied to fit against IXS data, and the dispersion relations were obtained from the fitting results.<sup>37</sup>

## 2.6. Electrochemical Impedance Spectroscopy

The electrochemical impedance spectroscopy (EIS) measurements were performed in the temperature range from 295 to 433 K using CHI750E electrochemical workstation at frequencies from 1 MHz to 100 mHz with an amplitude of 5 mV. The electronic conductivity was measured by the direct current (DC) polarization analysis. The samples were ground into powder and then loaded into a 10 mm diameter mold with stainless steel films on both sides, and pressed at 2.5 tons for 3 min. For the test at each temperature, the samples were equilibrated for 30 min before testing in an oven. The ionic conductivity is calculated by the formula,  $\sigma = d/RA$ , where  $d$  is the thickness of the pellet,  $A$  is the area of the test plane, and  $R$  is the resistance value that is obtained by fitting the impedance plots to the equivalent circuit model.

## 2.7. Fabrication of All-Solid-State Batteries

The cathode mixtures were prepared by mixing  $\text{CsI}_3$  powder,  $\text{Ag}_8\text{GeS}_6$  powder, and conductive carbon with a weight ratio of 5:4:1. The Ag powder was used as the anode and  $\text{Ag}_8\text{GeS}_6$  powder was used as the electrolyte. The ASSBs were assembled in the following procedure: first, a piece of stainless-steel foil was loaded into the mold, and then 0.2 g of Ag powder was uniformly spread and pressed onto the surface; subsequently, 0.3 g of  $\text{Ag}_8\text{GeS}_6$  powder was uniformly spread and pressed onto the surface of Ag anode layer; finally, 35 mg of mixed composite cathode powder was loaded and pressed onto the surface of electrolyte layer, followed by another layer of stainless-steel foil. The mold was pressed at 2.5 tons for 3 min.

## 2.8. Chemical State and Thermal Analysis

X-ray photoelectron spectroscopy (XPS, ESCALAB 250Xi) was used to collect the surface chemical states of the samples. Differential scanning calorimetry (DSC) analysis was conducted by NETZSCH 3500 with a temperature range of 313–573 K in flowing  $\text{N}_2$  gas. The sound velocity was measured using a pulse receiver (Olympus-NDT) equipped with an oscilloscope (Keysight). The thermal diffusivity ( $D$ ) was measured using laser flash method (Netzsch LFA 467). The thermal conductivity ( $\kappa$ ) was calculated from  $\kappa = \rho DC_p$ , where  $\rho$  is the density and  $C_p$  is the heat capacity determined by the Dulong-Petit limit.

## 2.9. Reverse Monte Carlo Modeling

The Reverse Monte Carlo (RMC) modeling was carried out with the RMCProfile software<sup>38,39</sup> using a  $4 \times 8 \times 6$  supercell of  $Pna2_1$  structure ( $60.596 \text{ \AA} \times 59.808 \text{ \AA} \times 63.534 \text{ \AA}$ ) containing 11,520 atoms. The synchrotron X-ray PDF  $G(r)$  and scattering function  $F(Q)$  data were used to fit the RMC model simultaneously. During the modeling process, all atoms were allowed to refine freely. Only a distance window and a minimum distance were applied as constraints in the refinements to retain  $[\text{GeS}_4]^{4-}$  polyhedra and prevent unphysical interatomic distances (Table S1). The simulation ran for

600 min on a 64-core CPU with a 2.4 GHz base frequency. Finally, the RMC fitting generated more than  $7.0 \times 10^6$  moves.

## 3. RESULTS AND DISCUSSION

### 3.1. Long-Range Structure

The temperature-dependent XRD and DSC results both confirm that the phase transition of the as-synthesized  $\text{Ag}_8\text{GeS}_6$  material occurs at 500 K, matching well with the literature,<sup>40</sup> as shown in Figures 1a and S1. The chemical states of Ag, Ge, and S are revealed to be +1, +4, and -2 by XPS, respectively (Figure S2), indicating the purity of the sample. The low-temperature phase is an orthorhombic structure with a space group of  $Pna2_1$  formed by the close-packed  $[\text{GeS}_4]^{4-}$  and  $\text{S}^{2-}$  anion rigid frameworks, with loosely bonded  $\text{Ag}^+$  ions.<sup>41</sup> The  $\text{Ag}^+$  ion sites have full occupancies in the low-temperature structure, possessing three different coordination environments, i.e., the tetrahedral, trigonal planar, and linear coordination with  $\text{S}^{2-}$  ions (Figure 1c). Notably, in these tetrahedrons,  $\text{Ag}^+$  ions shift slightly from the center, leading to structural distortions. When heated above 500 K,  $\text{Ag}_8\text{GeS}_6$  transforms to cubic  $F43m$  phase, forming the so-called superionic phase.<sup>41</sup> The  $\text{S}^{2-}$  ions at the  $16e$  position coordinate with Ge atoms to form  $[\text{GeS}_4]^{4-}$  tetrahedra, constituting the structural framework, while the remaining  $\text{S}^{2-}$  ions occupy the  $4a$  and  $4c$  positions. The  $\text{Ag}^+$  ions are distributed across two  $48h$  sites and one  $96i$  site, forming triangular and tetrahedral coordination with  $\text{S}^{2-}$ , respectively. Unlike the fully occupied cation site distribution in the low-temperature phase, the  $\text{Ag}^+$  ions in the high-temperature superionic phase are disordered, partially occupying three different crystallographic sites (Figure 1d).

To study the long-range crystallographic structure, the Rietveld refinements were carried out against the experimental XRD patterns (Figure S3). The detailed refinement results of low-temperature orthorhombic and high-temperature cubic phases are listed in Tables S2–S7. From the refinement results, the lattice parameters gradually increase with temperature, indicating the thermal expansion (Figures 1b and S4). The isotropic atomic displacement parameters ( $U_{iso}$ ) of Ag atoms from low-temperature data are larger than those of Ge and S atoms, indicating weak Ag–S bonds, which result in low sound velocity (Table S8).

The  $\text{Ag}^+$  ions randomly occupy the Ag1–Ag3 sites in the superionic phase, forming a disordered cubic structure as discussed above. The partially occupied cation sites enable the cations to hop into the adjacent vacant sites, and the 2D electron density maps indicate that the electron distribution of Ag atoms becomes overlapped upon heating, implying the Ag-ion diffusion (Figure 1e,f), which has been observed in other argyrodites.<sup>12,13,15,42</sup>

### 3.2. Local Structure and Thermal Conductivity

Sufficient structural disordering was observed in argyrodites as reported,<sup>12,43</sup> but unfortunately, conventional X-ray diffraction is incapable of analyzing the information beyond Bragg peaks. The PDF method is a local structure characterization method based on total scattering, which analyzes both Bragg and diffuse scattering signals.

The synchrotron X-ray experimental PDF data of polycrystalline  $\text{Ag}_8\text{GeS}_6$  were collected at room temperature, and the low-temperature crystal structure was used for PDF structural refinements. The PDF fit over the low- $r$  range of 1.8 Å to 11.8 Å is shown in Figure 2a, where the first peak (2.6

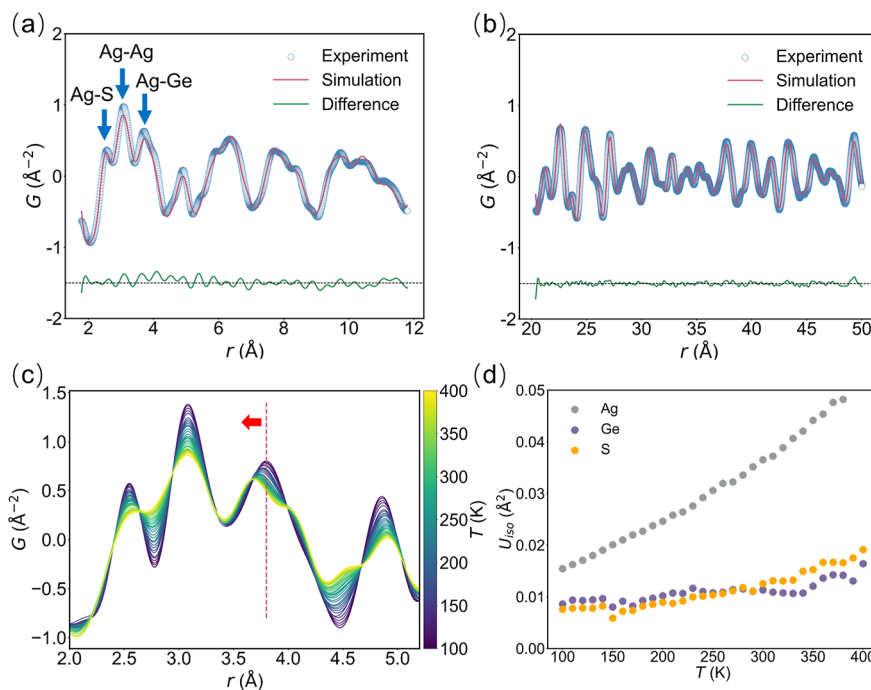


**Figure 2.** Room-temperature experimental X-ray PDF data (blue) are fit by the  $\text{Ag}_8\text{GeS}_6$  low-temperature  $Pna2_1$  phase model (red) over the range of (a)  $1.8 < r < 11.8 \text{ \AA}$ , in which the first three peaks represent Ag–S, Ag–Ag, and Ag–Ge bonds, respectively; (b)  $20.4 < r < 50.0 \text{ \AA}$ . The difference curve (green) is shown offset below. (c) Temperature-dependent X-ray PDF data from 100 to 400 K with 10 K interval. (d) Isotropic atomic displacement parameters of different types of atoms extracted from the temperature-dependent X-ray PDF refinements over the range of  $2.0 < r < 20.0 \text{ \AA}$ .

$\text{\AA}$ ) represents the nearest Ag–S bond length, the second peak ( $3.1 \text{ \AA}$ ) refers to the Ag–Ag bond length, and the third peak ( $3.7 \text{ \AA}$ ) is mainly from the Ag–Ge bond length. For the longer  $r$  range of  $20.4 \text{ \AA}$  to  $50.0 \text{ \AA}$  (Figure 2b), the averaged periodic atomic arrangements are in good agreement with the crystalline orthorhombic structure reported from literature,<sup>41</sup> indicating that the as-synthesized material is of high quality, and the average structure reconciles with the XRD results. The detailed PDF structural refinement results can be found in Tables S9 and S10. Notably, the PDF fit residual signals over the low- $r$  range, as shown in Figure 2a, suggest that the local structure is complicated due to the diffuse scattering, which is omitted in conventional XRD Bragg peak analysis.

To investigate the local structure evolution with temperature, the temperature-dependent PDF measurements were performed in  $\text{Ag}_8\text{GeS}_6$ . The peaks are broadened due to stronger thermal vibrations with temperature, which is accompanied by the decrease of peak intensities (Figure 2c). Meanwhile, the second PDF peak ( $3.1 \text{ \AA}$ ), which mainly represents Ag–Ag atom pairs, becomes asymmetric upon heating (Figure S5a). The non-Gaussian asymmetric peak can be explained by the anharmonicity of atomic motions,<sup>44,45</sup> which can be attributed to Ag atoms in this system. The peak at around  $3.7 \text{ \AA}$  splits into two peaks and shifts to the low- $r$  region (Figures 2c and S6). The partial PDFs show that this peak is mainly attributed to Ag–Ge atom pairs with a minor contribution from Ag–Ag pairs ( $\sim 4 \text{ \AA}$ ) (Figure S7). Therefore, the decreasing Ag–Ge distances and increasing Ag–Ag distances result in the peak split observed in PDF data.

When viewed from the local bonding environment, the Ge–S bonds change slowly with temperature, while Ag–S atom pairs are broadened significantly (Figure S5b,c). Based on the quantitative PDF local structure refinement, the isotropic

atomic displacement parameters (ADPs) of Ag atoms are much larger than those of Ge and S atoms (Figure 2d). These results indicate the weak bonding of Ag–S along with rigid  $[\text{GeS}_4]^{4-}$  units. Therefore, it is possible that the change in Ag–S bonds may lead to the change of the Ag–Ge atom pairs with temperature, which indicates the existence of local structural distortions.

This complex structural evolution may result in exotic thermal transport behaviors. The corresponding temperature-dependent thermal conductivity was measured, as shown in Figure S8. The contribution of electronic thermal conductivity to the measured total thermal conductivity is expected to be small in this system.<sup>46</sup> Therefore, the total thermal conductivity is nearly equal to the lattice thermal conductivity. The measured thermal conductivity of  $\text{Ag}_8\text{GeS}_6$  is  $0.367 \text{ W/m}\cdot\text{K}$  at  $300 \text{ K}$ , showing a low thermal conductivity and weak temperature dependence, similar to other Ag/Cu-based argyrodites.<sup>8,10,15,47–50</sup> To further study the structural dynamics of low thermal conductivity, the IXS experiment was carried out at the BL3SXU beamline of SPring-8. In Figures S9 and S10, the inelastic peaks shift to higher energy from  $\Gamma$  to L, accompanied by the peak broadening. The experimental results are consistent with the calculated phonon spectra.<sup>46</sup> This reveals strong lattice anharmonicity and shortening of the phonon relaxation time in this material,<sup>51</sup> which induces the intrinsically low lattice thermal conductivity.<sup>17,46,52</sup>

### 3.3. Three-Dimensional Diffuse Scattering Visualization

To fully understand the atomic arrangement beyond long-range Bragg peaks, we performed the synchrotron X-ray 3D total scattering experiment in argyrodites for the first time. This newly developed 3D PDF method can measure and visualize the diffuse scattering in the 3D space in a

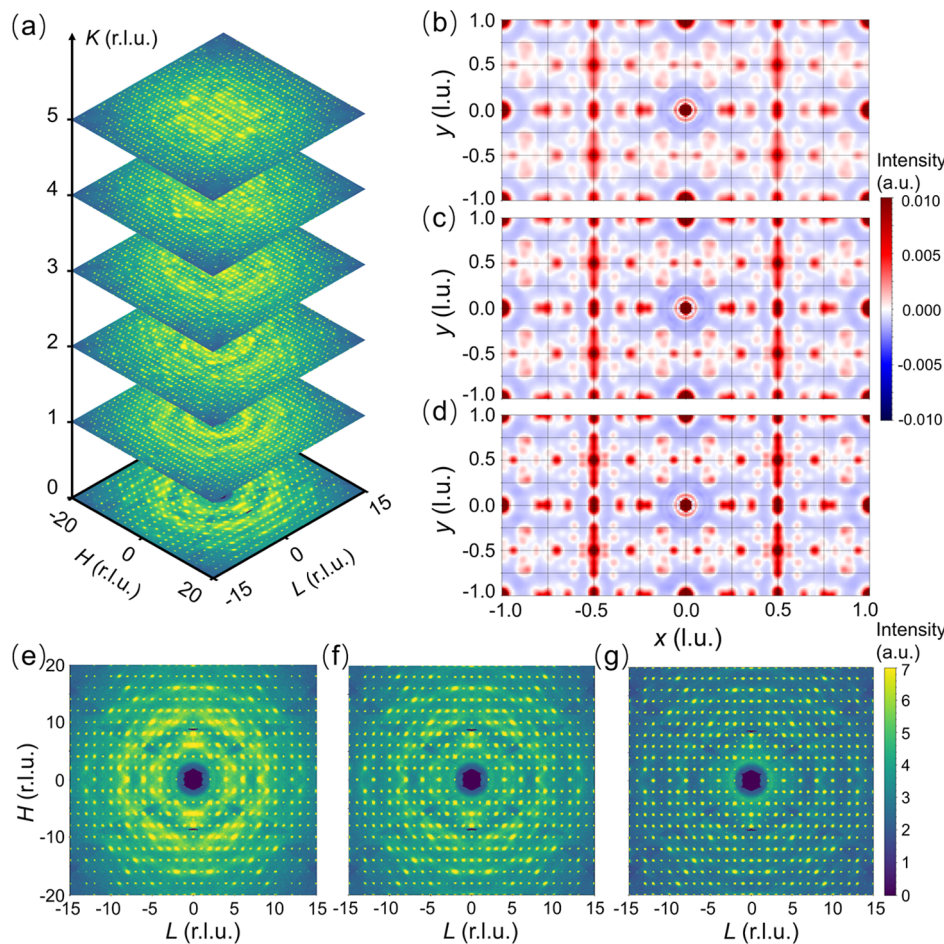


**Figure 3.** (a) Experimental three-dimensional volumes of X-ray diffuse scattering of the  $\text{Ag}_8\text{GeS}_6$  single crystal in the full reciprocal space  $Q = (HKL)$  planes at 300 K. (b-d) 3D total PDF in the  $(xy0)$  planes at (b) 300 K, (c) 200 K, and (d) 100 K, displayed in lattice units (l.u.), i.e., units of  $a$ ,  $b$ , and  $c$  along the  $x$ ,  $y$ , and  $z$  directions, respectively. (e-g) Diffuse scattering in the  $Q = (HOL)$  planes at (e) 300 K, (f) 200 K, and (g) 100 K, displayed in reciprocal lattice units (r.l.u.).

straightforward way. For  $\text{Ag}_8\text{GeS}_6$  single crystals, the experiments were performed at the BL02B1 beamline of SPring-8, which collects both Bragg and diffuse scattering over the full 3D reciprocal space  $HKL$ , as shown in Figures 3, S11, and S12. From the  $(HOL)$  slice, high-intensity bright Bragg spots in the reciprocal space were observed and they follow the extinction rule derived from the  $Pna_2$  crystal structure, showing that the long-range structure of synthesized single crystals is in good agreement with the literature.<sup>41</sup> Besides the Bragg spots, strong diffuse scattering signals in the orthorhombic phase were observed in the reciprocal space. The appearance of diffuse scattering signals suggests that the local structure of the material indeed deviates from the average structure, highlighting the structural complexity. Through the in situ temperature-dependent experiment (100–300 K), we found that the intensity and distribution of diffuse scattering are highly related to thermal motions (Figure 3b–d), and the thermal diffuse scattering signals become stronger when temperature increases, which is caused by the stronger atomic disordering in the local structure. Since large ADPs of Ag atoms have been revealed in the one-dimensional PDF analysis, the atomic disordering induced diffuse scattering is mainly contributed by the Ag atoms, whereas Ge and S atoms remain fairly stable. This three-dimensional X-ray diffuse scattering method provides a straightforward way to visualize

the diffuse scattering in argyrodites, which arises from the local structure disordering at the Ag atom sites. The strong diffuse scattering signals provide the direct structural evidence for the intrinsically low thermal conductivity of  $\text{Ag}_8\text{GeS}_6$ .

### 3.4. Superionic Phase Transition

To study the local structure in both low-temperature phase and high-temperature superionic phase, the X-ray PDF measurements were carried out using the high-temperature furnace at the BL04B2 beamline of SPring-8. The PDF data sets were collected at both 423 and 673 K, i.e., below and above the phase transition (500 K), respectively. As shown in Figure 4a,b, the PDF curves are different, indicating the phase transition of  $\text{Ag}_8\text{GeS}_6$ , which agrees with the literature report.<sup>40</sup> For the high-temperature PDF data (673 K), structural refinement was carried out over the range of 2.0–50.0 Å in real space using the high-temperature phase (space group  $F\bar{4}3m$ ). As shown in Figure 4c,d, the high-temperature phase fits well over the long range. But surprisingly, the high-temperature phase could not describe the local short-range structure at all, showing large misfits over the low- $r$  region. Studies on Li-based argyrodites have shown that similar local distortions exist beyond the average structure. Previous X-ray PDF analysis revealed that  $[\text{PS}_4]^{3-}$  tetrahedra in  $\text{Li}_6\text{PS}_5\text{X}$  ( $\text{X} = \text{Cl}, \text{Br}, \text{I}$ ) exhibit tilting and rotational disorder, and the

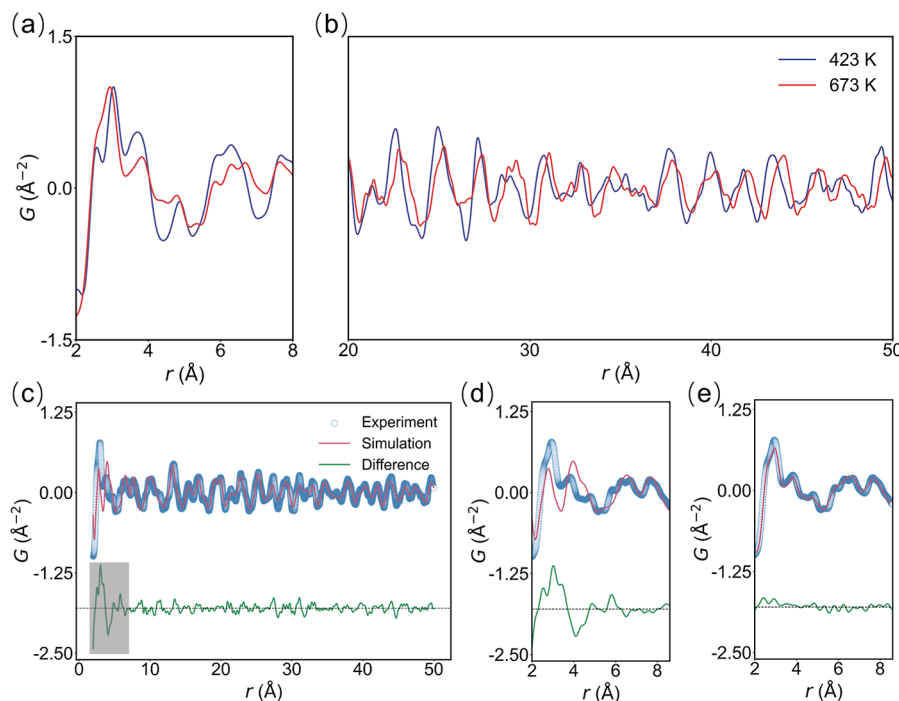


**Figure 4.** (a,b) The experimental X-ray PDF data collected at 423 and 673 K, i.e., below and above the phase transition (500 K). (c) The experimental X-ray PDF data (blue) at 673 K are fit by the high-temperature  $\text{Ag}_8\text{GeS}_6 F\bar{4}3m$  phase model (red) over the range of  $2.0 < r < 50.0 \text{ \AA}$ , and (d) enlarged part in the  $r$  range of  $2.0$ – $8.6 \text{ \AA}$ . (e) The experimental X-ray PDF data (blue) at 673 K are fit by the  $\text{Ag}_8\text{GeS}_6$  low-temperature  $Pna2_1$  phase model (red) over the range of  $2.0 < r < 8.6 \text{ \AA}$ .

distortions can be averaged into cubic symmetry at a longer length scale.<sup>53,54</sup>

To better investigate the local structure at high temperatures, we then tried to fit only the low- $r$  PDF data range ( $2.0$ – $8.6 \text{ \AA}$ ) (Figure 4e and Table S11). Remarkably, the low-temperature phase can fit the short-range atomic arrangement well. This can be explained by the similarity between the low-temperature and high-temperature phases. From the high-temperature high-symmetry phase to the low-temperature low-symmetry phase, the Ge and S atoms slightly deviate from the high-symmetry sites, inducing only a slight lattice distortion. Actually, the low-temperature structure could be approximated as a structure distorted from the high-temperature phase.

To gain further insights into this local structural distortion, we constructed a supercell built by low-temperature phase units through the RMC method.<sup>38,39</sup> The supercell model successfully captured both local and average structural behaviors, as shown in Figure S13. This suggests that the local structure persists as low-temperature phase up to at least 673 K, which is well above the average structure phase transition (500 K). The box-car PDF refinements were carried out over different  $r$  ranges (Figure S14), and the results indicate that the correlation length of the local structure is about 26 Å, i.e., within about 2 unit cells.

The supercell results indicate that  $[\text{GeS}_4]^{4-}$  tetrahedra exhibit significant distortions (Figure S15), which are possibly due to tilting as reported in Li-argyrodites.<sup>53</sup> The local structural distortions deviate from the long-range cubic symmetry, which cannot be observed by conventional Bragg diffraction. However, this distortion can be averaged into a cubic symmetry over a longer  $r$  range, thereby preserving a cubic periodicity in the long-range order. The  $[\text{GeS}_4]^{4-}$  tetrahedra exhibit distortions at high temperature from RMC results, which are also observed in the low-temperature  $Pna2_1$

phase (Figure S15). This indicates that local distortions are similar across the phase transition, which may help us understand the similar thermal conductivity below and above the phase transition.

In addition, we validate the similar local structural distortions in other Ag-based argyrodites. The  $\text{Ag}_9\text{GaSe}_6$  (phase transition  $\sim 281 \text{ K}$ )<sup>55</sup> and  $\text{Ag}_8\text{GeTe}_6$  (phase transition  $\sim 244 \text{ K}$ )<sup>56</sup> polycrystalline samples were tested by the X-ray PDF measurement. Similar local symmetry breaking phenomena are observed (Figures S16 and S17), revealing that the local structure cannot be described by the high-temperature superionic phase (space group:  $F\bar{4}3m$ ),<sup>57,58</sup> leaving large misfits at low- $r$  regions. This surprisingly similar result suggests that the exotic local structure behavior may commonly exist in the argyrodite family.

To cross-check the PDF analysis results, the data collected in a separate X-ray PDF experiment, at a different synchrotron facility, are shown in Figures S18 and S19 and Tables S12 and S13. The PDF analysis of these data confirms the observation from the main experiment presented in Figure 4.

### 3.5. Ion Transport Behavior

The high-temperature superionic phases of Ag/Cu-based argyrodites are known as ionic conductors.<sup>14,20</sup> Inspired by the local structural similarity in our analysis, the possible  $\text{Ag}^+$  ion transport in the low-temperature phase is studied accordingly. The temperature-dependent impedance spectroscopy was performed. The impedance response for  $\text{Ag}_8\text{GeS}_6$  is shown in Figure 5a, and other temperature data can be found in Figure S20. The data are fitted by an equivalent circuit, consisting of a series combination of bulk resistance ( $R_1$ ) and a parallel network of interfacial resistance ( $R_2$ ) with constant phase element ( $CPE_1$ ), further connected in series with a Warburg impedance ( $W_1$ ). The resulting ionic conductivity of

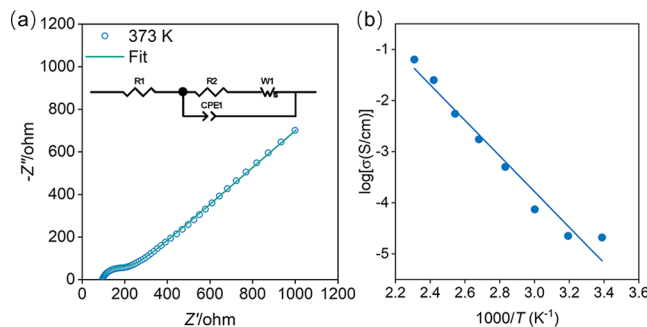


**Figure 5.** (a) Nyquist plot of  $\text{Ag}_8\text{GeS}_6$  at 373 K, along with the fitted equivalent circuits (insets). (b) Temperature-dependent ionic conductivities of  $\text{Ag}_8\text{GeS}_6$ .

$\text{Ag}_8\text{GeS}_6$  is 0.02 mS/cm at room temperature, which increases with temperature, reaching 63.7 mS/cm at 433 K. The electronic conductivity measured by DC polarization is  $9.7 \times 10^{-4}$  mS/cm at room temperature (Figure S21), and the corresponding transference number is 0.95, indicating it to be a promising Ag-ion conductor. The temperature-dependent ionic conductivity was evaluated by the Arrhenius formula, and the Arrhenius plots are shown in Figure 5b. The activation energy  $E_a$  is calculated by the Arrhenius formula:  $\sigma T = \sigma_0 \exp(-E_a/k_B T)$ , where  $\sigma_0$  is the prefactor. The calculated  $\sigma_0$  is  $4.66 \times 10^6 \text{ K}\cdot\text{S}/\text{cm}$  and the activation energy is  $0.69 \pm 0.05 \text{ eV}$ , which is higher than that of other insulating materials exhibiting  $\text{Ag}^+$  ion conduction, such as  $\text{AgI}$  ( $E_a = 0.10 \text{ eV}$ )<sup>59</sup> and  $\text{AgCrSe}_2$  ( $E_a = 0.11 \text{ eV}$ )<sup>60</sup> while being comparable to  $\text{AgGaGe}_3\text{Se}_8$  ( $E_a = 0.58 \text{ eV}$ )<sup>61</sup> and  $\text{AgGaS}_2$  ( $E_a = 0.62 \text{ eV}$ )<sup>62</sup>.

To demonstrate the potential application of  $\text{Ag}_8\text{GeS}_6$  solid-state electrolyte, the corresponding ASSBs were assembled and the electrochemical performance was assessed by galvanostatic charge/discharge method at a current density of 1.14 mA/g at 333 K. The charge and discharge profiles are sloping with a specific capacity of 15.80 mAh/g (Figure S22). The  $dQ/dV$  curve shows a pair of redox peaks at 0.68/0.58 V, indicating a solid solution reaction for the Ag-ion storage in  $\text{CsI}_3$ . Therefore, the low-temperature  $\text{Ag}_8\text{GeS}_6$  phase could enable the ASSB to operate, supporting the local structure analysis above. This work demonstrates the application of Ag-based argyrodites as solid-state electrolytes and largely expands the candidate search of ASSB electrolytes by examining the local structure behavior, which was usually omitted before if only focusing on long-range crystalline structures. This is the first report of an ASSB using Ag-based argyrodites, providing a complete workflow linking local structure analysis to property and performance testing.

#### 4. CONCLUSIONS

The local atomic structure of Ag-based argyrodites and its evolution with temperature have been investigated by the synchrotron X-ray atomic PDF method. The PDF analysis gives the short-range atomic arrangements beyond crystallographic structure, and the local symmetry breaking is revealed in  $\text{Ag}_8\text{GeS}_6$  and Ag-based argyrodite family materials. The weak bonding environment, strong lattice anharmonicity, and local structural distortion lead to the intrinsically low thermal conductivity in  $\text{Ag}_8\text{GeS}_6$ , as indicated by the significant diffuse scattering signals. In addition, the similarity between the low-temperature and high-temperature phases provides key insights into ion transport in the non-superionic phase. Furthermore,

all solid-state batteries employing  $\text{Ag}_8\text{GeS}_6$  have demonstrated its feasibility as a solid-state electrolyte. This strategy, motivated by local structure analysis, can serve as a novel screening approach for developing advanced functional materials.

#### ■ ASSOCIATED CONTENT

##### SI Supporting Information

The Supporting Information is available free of charge at <https://pubs.acs.org/doi/10.1021/jacs.Sc17193>.

Details of sample synthesis, PDF experiments, synchrotron X-ray diffraction experiments, XRD Rietveld refinement results, PDF refinement results, DSC results, XPS results, thermal conductivity results, IXS results, 3D total scattering results, RMC results, temperature-dependent EIS results, and charge/discharge curves of ASSBs (PDF)

#### ■ AUTHOR INFORMATION

##### Corresponding Author

**Long Yang** – Interdisciplinary Materials Research Center, School of Materials Science and Engineering, Tongji University, Shanghai 201804, China; [orcid.org/0000-0001-8731-0172](https://orcid.org/0000-0001-8731-0172); Email: [long\\_yang@tongji.edu.cn](mailto:long_yang@tongji.edu.cn)

##### Authors

**Te Kang** – Interdisciplinary Materials Research Center, School of Materials Science and Engineering, Tongji University, Shanghai 201804, China

**Changyuan Li** – Interdisciplinary Materials Research Center, School of Materials Science and Engineering, Tongji University, Shanghai 201804, China

**Xinjue Zhang** – Interdisciplinary Materials Research Center, School of Materials Science and Engineering, Tongji University, Shanghai 201804, China

**Yuiga Nakamura** – Diffraction and Scattering Division, Japan Synchrotron Radiation Research Institute, Sayo-gun, Hyogo 679-5198, Japan; [orcid.org/0000-0003-3696-0997](https://orcid.org/0000-0003-3696-0997)

**Jo-chi Tseng** – Diffraction and Scattering Division, Japan Synchrotron Radiation Research Institute, Sayo-gun, Hyogo 679-5198, Japan

**Taishun Manjo** – Precision Spectroscopy Division, Japan Synchrotron Radiation Research Institute SPring-8, Sayo-gun, Hyogo 679-5198, Japan

**Chaofeng Liu** – Interdisciplinary Materials Research Center, School of Materials Science and Engineering, Tongji University, Shanghai 201804, China; [orcid.org/0000-0003-2942-1418](https://orcid.org/0000-0003-2942-1418)

Complete contact information is available at:

<https://pubs.acs.org/10.1021/jacs.Sc17193>

##### Author Contributions

<sup>†</sup>T.K. and C.L. contributed equally to this work.

##### Notes

The authors declare no competing financial interest.

#### ■ ACKNOWLEDGMENTS

This work is supported by the National Natural Science Foundation of China (Grant No. 52302193 and 52472238), and the Fundamental Research Funds for the Central

Universities. We thank Prof. Yanzhong Pei for helpful discussions on thermal properties. The synchrotron radiation PDF experiments were performed at BL02B1, BL04B2, and BL08W of SPring-8 with the approval of Japan Synchrotron Radiation Research Institute (JASRI, Proposal No. 2024A1878, 2024A1375, and 2023A1347). The inelastic X-ray scattering experiments were performed at BL35XU of SPring-8. The authors thank the staff of beamline BL12SW at Shanghai Synchrotron Radiation Facility for X-ray PDF experiment supports.

## ■ REFERENCES

- (1) Famprakis, T.; Canepa, P.; Dawson, J. A.; Islam, M. S.; Masquelier, C. Fundamentals of Inorganic Solid-State Electrolytes for Batteries. *Nat. Mater.* **2019**, *18* (12), 1278–1291.
- (2) Janek, J.; Zeier, W. G. A Solid Future for Battery Development. *Nat. Energy* **2016**, *1* (9), 16141.
- (3) Gorochov, O. Les Composes  $\text{Ag}_8\text{MX}_6$  ( $\text{M} = \text{Si}, \text{Ge}, \text{Sn}$  et  $\text{X} = \text{S}, \text{Se}, \text{Te}$ ). *Bull. Soc. Chim. Fr.* **1968**, *6*, 2263–2275.
- (4) Kuhs, W. F.; Nitsche, R.; Scheunemann, K. The Argyrodites—A New Family of Tetrahedrally Close-Packed Structures. *Mater. Res. Bull.* **1979**, *14* (2), 241–248.
- (5) Hanghofer, I.; Gadermaier, B.; Wilkening, H. M. R. Fast Rotational Dynamics in Argyrodite-Type  $\text{Li}_6\text{PS}_5\text{X}$  ( $\text{X}: \text{Cl}, \text{Br}, \text{I}$ ) as Seen by  $^{31}\text{P}$  Nuclear Magnetic Relaxation—On Cation–Anion Coupled Transport in Thiophosphates. *Chem. Mater.* **2019**, *31* (12), 4591–4597.
- (6) Deiseroth, H.; Kong, S.; Eckert, H.; Vannahme, J.; Reiner, C.; Zaiß, T.; Schlosser, M.  $\text{Li}_6\text{PS}_5\text{X}$ : A Class of Crystalline Li-Rich Solids With an Unusually High  $\text{Li}^+$  Mobility. *Angew. Chem., Int. Ed.* **2008**, *47* (4), 755–758.
- (7) Chen, H. M.; Maohua, C.; Adams, S. Stability and Ionic Mobility in Argyrodite-Related Lithium-Ion Solid Electrolytes. *Phys. Chem. Chem. Phys.* **2015**, *17* (25), 16494–16506.
- (8) Weldert, K. S.; Zeier, W. G.; Day, T. W.; Panthöfer, M.; Snyder, G. J.; Tremel, W. Thermoelectric Transport in  $\text{Cu}_7\text{PSe}_6$  with High Copper Ionic Mobility. *J. Am. Chem. Soc.* **2014**, *136* (34), 12035–12040.
- (9) Lin, S.; Li, W.; Pei, Y. Thermally Insulative Thermoelectric Argyrodites. *Mater. Today* **2021**, *48*, 198–213.
- (10) Acharya, S.; Pandey, J.; Soni, A. Enhancement of Power Factor for Inherently Poor Thermal Conductor  $\text{Ag}_8\text{GeSe}_6$  by Replacing Ge with Sn. *ACS Appl. Energy Mater.* **2019**, *2* (1), 654–660.
- (11) Jin, Z.; Xiong, Y.; Zhao, K.; Dong, H.; Ren, Q.; Huang, H.; Qiu, X.; Xiao, J.; Qiu, P.; Chen, L.; Shi, X. Abnormal Thermal Conduction in Argyrodite-Type  $\text{Ag}_9\text{FeS}_6\text{-Te}$  Materials. *Mater. Today Phys.* **2021**, *19*, 100410.
- (12) Ren, Q.; Gupta, M. K.; Jin, M.; Ding, J.; Wu, J.; Chen, Z.; Lin, S.; Fabelo, O.; Rodríguez-Velamazán, J. A.; Kofu, M.; Nakajima, K.; Wolf, M.; Zhu, F.; Wang, J.; Cheng, Z.; Wang, G.; Tong, X.; Pei, Y.; Delaire, O.; Ma, J. Extreme Phonon Anharmonicity Underpins Superionic Diffusion and Ultralow Thermal Conductivity in Argyrodite  $\text{Ag}_8\text{SnSe}_6$ . *Nat. Mater.* **2023**, *22* (8), 999–1006.
- (13) Shen, X.; Koza, M. M.; Tung, Y.; Ouyang, N.; Yang, C.; Wang, C.; Chen, Y.; Willa, K.; Heid, R.; Zhou, X.; Weber, F. Soft Phonon Mode Triggering Fast Ag Diffusion in Superionic Argyrodite  $\text{Ag}_8\text{GeSe}_6$ . *Small* **2023**, *19* (49), 2305048.
- (14) Ghata, A.; Bernges, T.; Maus, O.; Wankmiller, B.; Naik, A. A.; Bustamante, J.; Gaulois, M. W.; Delaire, O.; Hansen, M. R.; George, J.; Zeier, W. G. Exploring the Thermal and Ionic Transport of  $\text{Cu}^+$  Conducting Argyrodite  $\text{Cu}_7\text{PSe}_6$ . *Adv. Energy Mater.* **2024**, *14* (46), 2402039.
- (15) Shen, X.; Ouyang, N.; Huang, Y.; Tung, Y.; Yang, C.; Faizan, M.; Perez, N.; He, R.; Sotnikov, A.; Willa, K.; Wang, C.; Chen, Y.; Guilmeau, E. Amorphous-Like Ultralow Thermal Transport in Crystalline Argyrodite  $\text{Cu}_7\text{PS}_6$ . *Adv. Sci.* **2024**, *11* (22), 2400258.
- (16) Schwarzmüller, S.; Souchay, D.; Günther, D.; Gocke, A.; Dovgaliuk, I.; Miller, S. A.; Snyder, G. J.; Oeckler, O. Argyrodite-Type  $\text{Cu}_8\text{GeSe}_{6-x}\text{Te}_x$  ( $0 \leq x \leq 2$ ): Temperature-Dependent Crystal Structure and Thermoelectric Properties. *Z. Anorg. Allg. Chem.* **2018**, *644* (24), 1915–1922.
- (17) Jiang, B.; Qiu, P.; Chen, H.; Huang, J.; Mao, T.; Wang, Y.; Song, Q.; Ren, D.; Shi, X.; Chen, L. Entropy Optimized Phase Transitions and Improved Thermoelectric Performance in N-Type Liquid-like  $\text{Ag}_9\text{GaSe}_6$  Materials. *Mater. Today Phys.* **2018**, *5*, 20–28.
- (18) Li, W.; Lin, S.; Weiss, M.; Chen, Z.; Li, J.; Xu, Y.; Zeier, W. G.; Pei, Y. Crystal Structure Induced Ultralow Lattice Thermal Conductivity in Thermoelectric  $\text{Ag}_9\text{AlSe}_6$ . *Adv. Energy Mater.* **2018**, *8* (18), 1800030.
- (19) Lin, S.; Li, W.; Li, S.; Zhang, X.; Chen, Z.; Xu, Y.; Chen, Y.; Pei, Y. High Thermoelectric Performance of  $\text{Ag}_9\text{GaSe}_6$  Enabled by Low Cutoff Frequency of Acoustic Phonons. *Joule* **2017**, *1* (4), 816–830.
- (20) Bernges, T.; Hanus, R.; Wankmiller, B.; Imasato, K.; Lin, S.; Ghidu, M.; Gerlitz, M.; Peterlechner, M.; Graham, S.; Hautier, G.; Pei, Y.; Hansen, M. R.; Wilde, G.; Snyder, G. J.; George, J.; Agne, M. T.; Zeier, W. G. Considering the Role of Ion Transport in Diffusion-Dominated Thermal Conductivity. *Adv. Energy Mater.* **2022**, *12* (22), 2200717.
- (21) Billinge, S. J. L.; Skjaervoe, S. H.; Terban, M. W.; Tao, S.; Yang, L.; Rakita, Y.; Frandsen, B. A. Local Structure Determination Using Total Scattering Data. In *Comprehensive Inorganic Chemistry III*; Elsevier, 2023; pp 222–247.
- (22) Egami, T.; Billinge, S. J. L. *Underneath the Bragg Peaks: Structural Analysis of Complex Materials*, 2nd ed.; Pergamon Materials Series; Elsevier: Amsterdam, 2012.
- (23) Weber, T.; Simonov, A. The Three-Dimensional Pair Distribution Function Analysis of Disordered Single Crystals: Basic Concepts. *Z. Kristallogr.* **2012**, *227* (5), 238–247.
- (24) Krogstad, M. J.; Rosenkranz, S.; Wozniak, J. M.; Jennings, G.; Ruff, J. P. C.; Vaughey, J. T.; Osborn, R. Reciprocal Space Imaging of Ionic Correlations in Intercalation Compounds. *Nat. Mater.* **2020**, *19* (1), 63–68.
- (25) Toby, B. H.; Von Dreele, R. B. GSAS-II: The Genesis of a Modern Open-Source All Purpose Crystallography Software Package. *J. Appl. Crystallogr.* **2013**, *46* (2), 544–549.
- (26) Momma, K.; Ikeda, T.; Belik, A. A.; Izumi, F. Dysnomia, a Computer Program for Maximum-Entropy Method (MEM) Analysis and Its Performance in the MEM-Based Pattern Fitting. *Powder Diffr.* **2013**, *28* (3), 184–193.
- (27) Sakata, M.; Sato, M. Accurate Structure Analysis by the Maximum-Entropy Method. *Acta Crystallogr., Sect. A* **1990**, *46* (4), 263–270.
- (28) Momma, K.; Izumi, F. VESTA 3 for Three-Dimensional Visualization of Crystal, Volumetric and Morphology Data. *J. Appl. Crystallogr.* **2011**, *44* (6), 1272–1276.
- (29) Juhás, P.; Davis, T.; Farrow, C. L.; Billinge, S. J. L. PDFgetX3: A Rapid and Highly Automatable Program for Processing Powder Diffraction Data into Total Scattering Pair Distribution Functions. *J. Appl. Crystallogr.* **2013**, *46* (2), 560–566.
- (30) Kieffer, J.; Karkoulis, D. PyFAI, a Versatile Library for Azimuthal Regrouping. *J. Phys.: Conf. Ser.* **2013**, *425* (20), 202012.
- (31) Farrow, C. L.; Juhás, P.; Liu, J. W.; Bryndin, D.; Božin, E. S.; Bloch, J.; Proffen, T.; Billinge, S. J. L. PDFfit2 and PDFgui: Computer Programs for Studying Nanostructure in Crystals. *J. Phys.: Condens. Matter* **2007**, *19* (33), 335219.
- (32) Chupas, P. J.; Qiu, X.; Hanson, J. C.; Lee, P. L.; Grey, C. P.; Billinge, S. J. L. Rapid-Acquisition Pair Distribution Function (RA-PDF) Analysis. *J. Appl. Crystallogr.* **2003**, *36* (6), 1342–1347.
- (33) Proffen, Th.; Billinge, S. J. L. PDFFIT, a Program for Full Profile Structural Refinement of the Atomic Pair Distribution Function. *J. Appl. Crystallogr.* **1999**, *32* (3), 572–575.
- (34) Jeong, I.-K.; Proffen, T.; Mohiuddin-Jacobs, F.; Billinge, S. J. L. Measuring Correlated Atomic Motion Using X-Ray Diffraction. *J. Phys. Chem. A* **1999**, *103* (7), 921–924.
- (35) Jennings, G. *Crystal Coordinate Transformation Workflow (CCTW)*; SourceForge, 2019; . <https://sourceforge.net/projects/cctw/>.

- (36) Baron, A. Q. R.; Tanaka, Y.; Goto, S.; Takeshita, K.; Matsushita, T.; Ishikawa, T. An X-Ray Scattering Beamline for Studying Dynamics. *J. Phys. Chem. Solids* **2000**, *61* (3), 461–465.
- (37) Baron, A. Q. R. Phonons in Crystals Using Inelastic X-Ray Scattering. *J. Spectrom. Soc. Jpn.* **2009**, *58*, 205–214.
- (38) McGreevy, R. L. Reverse Monte Carlo Modelling. *J. Phys.: Condens. Matter* **2001**, *13* (46), R877–R913.
- (39) Tucker, M. G.; Dove, M. T.; Keen, D. A. Application of the Reverse Monte Carlo Method to Crystalline Materials. *J. Appl. Crystallogr.* **2001**, *34* (5), 630–638.
- (40) Pogodin, A. I.; Filep, M. J.; Izai, V. Yu.; Kokhan, O. P.; Kúš, P. Crystal Growth and Electrical Conductivity of  $\text{Ag}_7\text{PS}_6$  and  $\text{Ag}_8\text{GeS}_6$  Argyrodites. *J. Phys. Chem. Solids* **2022**, *168*, 110828.
- (41) Eulenberger, G. Die Kristallstruktur Der Tieftemperaturmodifikation von  $\text{Ag}_8\text{GeS}_6$  - Synthetischer Argyrodit. *Monatsh. Chem.* **1977**, *108* (4), 901–913.
- (42) Gupta, M. K.; Ding, J.; Bansal, D.; Abernathy, D. L.; Ehlers, G.; Osti, N. C.; Zeier, W. G.; Delaire, O. Strongly Anharmonic Phonons and Their Role in Superionic Diffusion and Ultralow Thermal Conductivity of  $\text{Cu}_2\text{PSe}_6$ . *Adv. Energy Mater.* **2022**, *12* (23), 2200596.
- (43) Takahashi, S.; Kasai, H.; Liu, C.; Miao, L.; Nishibori, E. Rattling of Ag Atoms Found in the Low-Temperature Phase of Thermoelectric Argyrodite  $\text{Ag}_8\text{SnSe}_6$ . *Cryst. Growth Des.* **2024**, *24* (15), 6267–6274.
- (44) Li, C. W.; Ma, J.; Cao, H. B.; May, A. F.; Abernathy, D. L.; Ehlers, G.; Hoffmann, C.; Wang, X.; Hong, T.; Huq, A.; Gourdon, O.; Delaire, O. Anharmonicity and Atomic Distribution of SnTe and PbTe Thermoelectrics. *Phys. Rev. B* **2014**, *90* (21), 214303.
- (45) Knox, K. R.; Bozin, E. S.; Malliakas, C. D.; Kanatzidis, M. G.; Billinge, S. J. L. Local Off-Centering Symmetry Breaking in the High-Temperature Regime of SnTe. *Phys. Rev. B* **2014**, *89* (1), 014102.
- (46) Ouyang, N.; Shen, D.; Wang, C.; Cheng, R.; Wang, Q.; Chen, Y. Positive Temperature-Dependent Thermal Conductivity Induced by Wavelike Phonons in Complex Ag-Based Argyrodites. *Phys. Rev. B* **2025**, *111* (6), 064307.
- (47) Shen, X.; Xia, Y.; Yang, C.; Zhang, Z.; Li, S.; Tung, Y.; Benton, A.; Zhang, X.; Lu, X.; Wang, G.; He, J.; Zhou, X. High Thermoelectric Performance in Sulfide-Type Argyrodites Compound  $\text{Ag}_x\text{Sn}(\text{S}_{1-x}\text{Se}_x)_6$  Enabled by Ultralow Lattice Thermal Conductivity and Extended Cubic Phase Regime. *Adv. Funct. Mater.* **2020**, *30* (21), 2000526.
- (48) Jin, M.; Lin, S.; Li, W.; Chen, Z.; Li, R.; Wang, X.; Chen, Y.; Pei, Y. Fabrication and Thermoelectric Properties of Single-Crystal Argyrodite  $\text{Ag}_8\text{SnSe}_6$ . *Chem. Mater.* **2019**, *31* (7), 2603–2610.
- (49) Jiang, B.; Qiu, P.; Chen, H.; Zhang, Q.; Zhao, K.; Ren, D.; Shi, X.; Chen, L. An Argyrodite-Type  $\text{Ag}_8\text{GaSe}_6$  Liquid-like Material with Ultralow Thermal Conductivity and High Thermoelectric Performance. *Chem. Commun.* **2017**, *53* (85), 11658–11661.
- (50) Lin, S.; Li, W.; Bu, Z.; Gao, B.; Li, J.; Pei, Y. Thermoelectric Properties of  $\text{Ag}_9\text{GaS}_6$  with Ultralow Lattice Thermal Conductivity. *Mater. Today Phys.* **2018**, *6*, 60–67.
- (51) Wang, T.; Dou, K.; Wang, H.; Kim, J.; Wang, X.; Su, W.; Chen, T.; Kim, W.; Wang, C. Higher-Order Anharmonicity Leads to Ultralow Thermal Conductivity and High Output Power Density of SnTe-Based Thermoelectric Materials and Modules. *Mater. Today Phys.* **2022**, *26*, 100748.
- (52) Li, W.; Lin, S.; Ge, B.; Yang, J.; Zhang, W.; Pei, Y. Low Sound Velocity Contributing to the High Thermoelectric Performance of  $\text{Ag}_8\text{SnSe}_6$ . *Adv. Sci.* **2016**, *3* (11), 1600196.
- (53) Schlenker, R.; Hansen, A.-L.; Senyshyn, A.; Zinkevich, T.; Knapp, M.; Hupfer, T.; Ehrenberg, H.; Indris, S. Structure and Diffusion Pathways in  $\text{Li}_6\text{PS}_5\text{Cl}$  Argyrodite from Neutron Diffraction, Pair-Distribution Function Analysis, and NMR. *Chem. Mater.* **2020**, *32* (19), 8420–8430.
- (54) Shotwell, A. M.; Schulze, M. C.; Yox, P.; Alaniz, C.; Maughan, A. E. Tetrahedral Tilting and Lithium-Ion Transport in Halide Argyrodites Prepared by Rapid, Microwave-Assisted Synthesis. *Adv. Funct. Mater.* **2025**, *35*, 2500237.
- (55) Tansho, M.; Wada, H.; Onoda, Y. Silver Ionic Conductor  $\text{Ag}_9\text{GaSe}_6$  Studied by Ag and Ga NMR. *Solid State Ionics* **1996**, *86*–88, 155–158.
- (56) Kawaji, H.; Atake, T. Heat Capacity Measurement and Thermodynamic Study of  $\text{Ag}_8\text{GeTe}_6$ . *Solid State Ionics* **1994**, *70*–71, 518–521.
- (57) Geller, S. The Crystal Structure of  $\gamma \text{Ag}_8\text{GeTe}_6$ , a Potential Mixed Electronic-Ionic Conductor. *Z. Kristallogr.* **1979**, *149* (1–2), 31–47.
- (58) Deloume, J.; Faure, R.; Loiseleur, H.; Roubin, M. Crystal Structure of the Phase  $\text{Ag}_9\text{GaSe}_6$  Beta. *Acta Crystallogr. B* **1978**, *34* (11), 3189–3193.
- (59) Allen, P. C.; Lazarus, D. Effect of Pressure on Ionic Conductivity in Rubidium Silver Iodide and Silver Iodide. *Phys. Rev. B* **1978**, *17* (4), 1913–1927.
- (60) Murphy, D. W.; Chen, H. S.; Tell, B. Superionic Conduction in  $\text{AgCrS}_2$  and  $\text{AgCrSe}_2$ . *J. Electrochem. Soc.* **1977**, *124* (8), 1268–1271.
- (61) Hellstrom, E. E.; Huggins, R. A. Silver Ionic and Electronic Conductivity in  $\text{Ag}_9\text{GaS}_6$ ,  $\text{Ag}_9\text{AlS}_6$ ,  $\text{AgGaS}_2$ ,  $\text{AgAlS}_2$ , and  $\text{AgAl}_5\text{S}_8$ . *J. Solid State Chem.* **1980**, *35* (2), 207–214.
- (62) Thorup, P. S.; Stubkjær, R. B.; Huynh, K.-K.; Ventrapati, P.; Vossgaard, E. S.; Borup, A. B.; Iversen, B. B. Structural Origins of Ultralow Glass-like Thermal Conductivity in  $\text{AgGaGe}_3\text{Se}_8$ . *Sci. Adv.* **2025**, *11* (24), 5865.

**CAS INSIGHTS™****EXPLORE THE INNOVATIONS SHAPING TOMORROW**

Discover the latest scientific research and trends with CAS Insights. Subscribe for email updates on new articles, reports, and webinars at the intersection of science and innovation.

**Subscribe today**